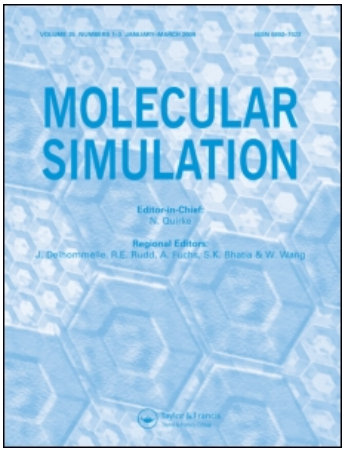

Molecular Simulation
Publication details, including instructions for authors and subscription information:
http://www.informaworld.com/smpp/title~content=t713644482

Isotherm and heat of adsorption in porous solids with defective pores—adsorption of argon and nitrogen at 77 K in Saran activated carbon

D. D. Do[a]; H. D. Do[a]
[a] Division of Chemical Engineering, University of Queensland, St Lucia, Qld, Australia

To cite this Article Do, D. D. and Do, H. D.(2007) 'Isotherm and heat of adsorption in porous solids with defective pores—adsorption of argon and nitrogen at 77 K in Saran activated carbon', Molecular Simulation, 33: 9, 821 — 837
To link to this Article: DOI: 10.1080/08927020701275043
URL: http://dx.doi.org/10.1080/08927020701275043

Molecular Simulation, Vol. 33, Nos. 9–10, 15–30 August 2007, 821–837

Taylor & Francis
Taylor & Francis Group

Isotherm and heat of adsorption in porous solids with defective pores—adsorption of argon and nitrogen at 77 K in Saran activated carbon

D. D. DO* and H. D. DO

Division of Chemical Engineering, University of Queensland, St Lucia, Qld 4072, Australia

(Received December 2006; in final form February 2007)

The isotherm and isosteric heat of a porous solid are studied in terms of the local isotherms and isosteric heats of individual pores with defective walls, rather than graphitic walls as commonly assumed in the literature. We point out the incorrect formulas that have been used in the literature, and present a correct formula to calculate the isosteric heat for a porous solid. The correct formula is illustrated with a direct Monte Carlo (MC) simulation of systems of two pores of different sizes, and finally we apply our theory to experimental data of argon and nitrogen adsorption at 77 K on S600H and S84 Saran charcoals to derive their pore size distributions (PSD). We show that the PSD derived from the fitting either the isotherm only or the heat curve only may not be reliable. It is necessary to utilize both the isotherm and heat curves in the derivation of a more reliable PSD. We also show that it is essential to use defected walls of carbon pores to model adsorption in pores as the model using graphitic walls can not describe isotherm and heat of adsorption adequately.

Keywords: Isotherm; Isosteric heat; Activated charcoal; Activated carbon

1. Introduction

Adsorption in porous solids has now been routinely carried out in all laboratories, using various methods such as the volumetric techniques, the gravimetric apparatus and the perturbation chromatography. Although isotherm data are readily obtained, the isosteric heat is not directly measured and this is acquired only in laboratories that are equipped with sensitive calorimeters. Research works on calorimetry by various workers in the past, notably by Beebe [1–12], Kiselev [13–33], Rouquerol [34–39], Aston [40–45], Morrison [46–60] and Pace [61–70], etc. have shed valuable information on the behavior of adsorption because the heat of adsorption is more sensitive to the system characteristics than the adsorption isotherm. It might be worthwhile to mention that these works were published in the 50–70. Although theoretical works (mostly apply the basic Clausius–Clapeyron equation) are abundantly available in the literature, experimental work on calorimetric measurement has been scarce. In the absence of experimental data on heat of adsorption, molecular simulation tools provide an alternative to provide this information. Monte Carlo (MC) method, in particular, has been used more frequently in the calculation of the isosteric heat. The following formula developed by Nicholson and Parsonage [71] is used by using the ensemble averages of various fluctuating quantities in the Grand Canonical and their combinations in the Markov chain.

$$q_{st} = \frac{\langle U\rangle\langle N\rangle - \langle UN\rangle}{\langle N^2\rangle - \langle N\rangle\langle N\rangle} + kT \tag{1}$$

where $\langle\rangle$ is the ensemble average, N is the number of particle and U is the configuration energy of the system. This configuration energy can be divided into two contributions, one is due to the fluid–fluid interaction while the other is to the fluid–solid interaction, that is $U = U_{ff} + U_{sf}$. The contribution to the heat due to the fluid–fluid interaction can be calculated from the first term in the RHS of equation (1) by replacing U by U_{ff}. Similarly, the contribution by the solid–fluid is obtained with U being replaced by U_{sf}. Equation (1) is easily applied in a Grand Canonical Monte Carlo (GCMC) simulation of a single pore of a given structural and chemical configuration. In the case of a porous solid

*Corresponding author. Tel.: + 61-7-3365-4154. Fax: + 61-7-3365-2789. Email: duongd@cheque.uq.edu.au

Molecular Simulation
ISSN 0892-7022 print/ISSN 1029-0435 online © 2007 Taylor & Francis
http://www.tandf.co.uk/journals
DOI: 10.1080/08927020701275043

having a distribution of independent pores, the isosteric heat of this porous solid at a given pressure is calculated from the following formula as proposed in the literature [72,73]

$$q_{\rm st}^{\rm porous}(p) = \frac{\sum_{j=1}^{N} \alpha_j \rho_j(p;H_j) q_{{\rm st},j}(p;H_j)}{\sum_{j=1}^{N} \alpha_j \rho_j(p;H_j)} \left[\frac{\rm mol}{\rm kg}\right] \quad (2)$$

where α_j is the specific volume (m^3/kg) of pores having a width H_j, ρ_j is the average density in this pore (mol/m^3) at the pressure p under consideration and $q_{{\rm st},j}$ is the isosteric heat (J/mol) of the same pore at the same pressure. This formula has been used by a number of workers [73] for studying of adsorption in porous carbons and also used in the derivation of pore size distribution (PSD), and we have shown that equation (2) is erroneous [74]. The obvious reason why this is wrong is that at high pressures where small pores have been completely filled, an addition of a molecule into the system will see that molecule enter larger pores. What this means is that the contribution of small pores to the isosteric heat of the porous solid is essentially zero. Unfortunately, this is not exactly what equation (2) suggests. Furthermore, we will show that using just the heat curve to derive the PSD is not adequate. At least we should use both isotherm and heat curve, or even better use the isotherms and heat curves of two different molecular probes, such as argon and nitrogen. We will illustrate this with the analysis of isotherms and heats of argon and nitrogen adsorption in Saran-activated charcoal S84 and S600H in the derivation of their PSDs.

2. Potential energy

2.1 Fluid–fluid potential energy

The interaction energy between two particles is calculated from the 12–6 Lennard–Jones potential equation:

$$\varphi_{i,j} = 4\varepsilon^{({\rm f,f})}\left[(\sigma^{({\rm f,f})}/r_{i,j})^{12} - (\sigma^{({\rm f,f})}/r_{i,j})^{6}\right] \quad (3)$$

where the subscript denotes particle, and $r_{i,j}$ is the distance between particles i and j. This equation is widely applied in fluid behavior and in adsorption of simple gases on graphitized thermal carbon black [75–77], whose simulation results agree well with experimental data [29,78]. The following values for the molecular parameters have been commonly used in the literature for argon [79] $\sigma = 3.405$ A and $\varepsilon/k = 119.8$ K and nitrogen [80], $\sigma = 3.615$ A and $\varepsilon/k = 101.5$ K and they will be used in this work.

2.2 Solid–fluid interaction energy

The surface is modeled as M layers of defective graphene sheets of discrete carbon atoms. For layers underneath the Mth layer, they are treated as structure-less layers. This is reasonable because the distance from the particle to the $(M+1)$th and underneath layers is much greater than the carbon–carbon bond length. To calculate the solid–fluid interaction with graphene layers below the defective layers, we use the classical 10—4—3 Steele potential [81]

$$\varphi_{i,{\rm s}} = 4\pi\rho_{\rm s}\varepsilon^{({\rm f,s})}[\sigma^{({\rm f,s})}]^2 \times \left\{\frac{1}{5}\left(\frac{\sigma^{({\rm f,s})}}{z_{i,{\rm s}}}\right)^{10} - \frac{1}{2}\left(\frac{\sigma^{({\rm f,s})}}{z_{i,{\rm s}}}\right)^{4} - \frac{[\sigma^{({\rm f,s})}]^4}{6\Delta(0.61\Delta + z_{i,{\rm s}})^3}\right\} \quad (4)$$

where $\rho_{\rm s}$ is the density of carbon atom per unit surface area of the graphene layer ($\rho_{\rm s} = 0.382\,{\rm A}^{-2}$), and Δ is the spacing between two adjacent layers (3.35 A). The solid–fluid molecular parameters, the collision diameter and the interaction energy, are calculated from the Lorentz–Berthelot mixing rule. The molecular parameters of a carbon atom in the graphite layer are: $\sigma^{({\rm s,s})} = 3.4$ A and $\varepsilon^{({\rm s,s})}/k = 28$ K. To calculate the solid–fluid potential between a particle and the top M defective layers, we sum the pairwise potentials between that particle and all carbon atoms in those layers.

2.3 Grand Canonical Monte Carlo simulation

In the GCMC simulation [82,83], we specify temperature, volume (pore volume) and the chemical potential. The parameters associated with the MC simulation used in this paper are (i) the box length is at least 10 times the collision diameter, (ii) the cut-off radius is half of the box length and (iii) the number of cycles for equilibration step and statistic collection is 1,000,000, and in each cycle we have N attempts of displacement move and N attempts of insertion/deletion of equal probability. These large numbers of cycle are necessary to obtain reliable isosteric heat as this variable has large fluctuations during the MC run.

Assuming that we know the *accessible* volume, V' (to be discussed in Section 3.2), which is defined as the volume that can be probed by a particle, the pore density is defined as:

$$\langle\rho\rangle = \langle N\rangle / V'. \quad (5)$$

The isosteric heat, which is the amount of energy released for each molecule added to the adsorbed phase at a given temperature and loading in the simulation box, is given in equation (1).

3. Model of a non-graphitized carbon surface

3.1 A new model for non-graphitized surface

The surface model for the pore wall is taken from the recent work of Do and Do [84], and we only describe it briefly here. The surface is modeled as a collection of graphene layers with the top M layers being defective. To model defects, we select a carbon atom in random and remove it as well as its neighbors whose distances to

the selected atom are less than R_c (hereafter called the effective defect radius). This is repeated until the percentage of carbon atoms removed has reached a specified value. Thus, the three structural parameters characterizing a defective surface are the number of defective layers, the percentage of defect and its effective defect radius. To minimize the model parameter in this paper, we use one defective top layer, and will study the effects of the other two parameters.

3.2 Accessible volume and "BET"-surface area

Having defined a slit pore with defective walls, it is necessary to calculate the accessible pore volume V' as this is required in the calculation of pore density (equation 5). We do this with a MC approach [84], in which we insert a particle into the simulation box and then remove it from the box. For each insertion, the solid–fluid potential is calculated, and if it is negative or zero, we count that insertion as a successful one. After a large number of insertions (Ten millions attempts are used in this work) the percentage of successful insertion is taken to be the ratio of the accessible volume to the volume of the simulation box. This accessible volume, V^*, is the volume that is available only to the *center* of a particle. Because a particle has a finite volume, we need to determine the accessible volume that is available to the whole particle. To do this, we adopt a simple geometrical consideration in that if we know the "surface area", we can determine the accessible volume for the whole particle as the sum of V^* and the extra volume accounting for the finite size of the adsorbate. This extra volume is $S\sigma$, where S is the surface area of one surface and σ is the collision diameter of the adsorbate. Here we adopt the "BET"- surface area which is derived from the GCMC simulation of nitrogen adsorption at 77 K. From this simulation, we obtain the number adsorbed as a function of pressure in the reduced pressure range from 0.05 to 0.30. Next we apply the linearized BET plot to determine the surface area with the molecular projection area of nitrogen of 16.2 A^2 [85]. Once this area, S, has been determined, we determine the accessible pore volume to the whole particle, $V' = V^* + S\sigma$.

4. Isosteric heat for porous solids having a pore size distribution

Recently we presented a correct formula [85] to calculate the isosteric heat for a porous solid. Here we present an alternative derivation, and apply a MC approach to illustrate the correct equation. To calculate the isosteric heat resulted from adsorption in a porous solid having a PSD, we start with this system under equilibrium at a given pressure p. At this pressure, the amount adsorbed per unit mass is

$$N(p) = \sum_{j=1}^{M} \rho(p; H_j)\alpha_j \tag{6}$$

where $\rho(p,H_j)$ is the average pore density in a pore having width H_j, and α_j is the volume of this pore per unit mass. The total specific volume (m^3/kg) of the porous solid is $\sum_{j=1}^{M}\alpha_j$. At the same pressure p, the isosteric heat in the pore H_j is $q_{st,j}(p)$. Traditionally the isosteric heat is presented as a function of loading. It is more appropriate, in the context of what we are doing here, to express it in terms of pressure.

When the pressure is increased from p to $p + dp$, the amount adsorbed in the porous solid is increased to $N(p + dp)$, which is obtained from equation (6) with p being replaced by $p + dp$. Thus, the increment in the amount adsorbed in the pore H_j is $\rho(p + dp;H_j) - \rho(p;H_j)$, and the corresponding increment of the total amount adsorbed is simply the sum of individual contributions from each pore:

$$\Delta N = N(p + dp) - N(p)$$

$$= \sum_{j=1}^{M} [\rho(p + dp, H_j) - \rho(p, H_j)]\alpha_j.$$

The additional heat released due to this increase in pressure is

$$\Delta Q = \sum_{j=1}^{M} [\rho(p + dp, H_j) - \rho(p, H_j)]\alpha_j q_{st}(p; H_j).$$

Therefore, the incremental molar heat of the porous solid is the ratio of the incremental heat to the incremental amount added to the system due to the incremental increase in pressure, dp

$$q_{st}(p) = \frac{\Delta Q}{\Delta N}$$

$$= \frac{\sum_{j=1}^{M} [\rho(p + \mathrm{d}p; H_j) - \rho(p; H_j)]\alpha_j q_{st}(p; H_j)}{\sum_{j=1}^{M} [\rho(p + \mathrm{d}p; H_j) - \rho(p; H_j)]\alpha_j}.$$

For an infinitesimally small change in pressure ($dp \to 0$), we apply the Taylor expansion to the above equation to finally obtain an expression for the isosteric heat in a porous solid as a function of pressure

$$q_{st}(p) = \lim_{dP \to 0} \frac{\Delta Q}{\Delta N} = \frac{\sum_{j=1}^{M} \alpha_j q_{st}(p; H_j) \frac{\partial \rho(p;H_j)}{\partial p}}{\sum_{j=1}^{M} \alpha_j \frac{\partial \rho(p;H_j)}{\partial p}}. \tag{7}$$

The above equation can also be derived by applying the Clapeyron–Clausius equation to the isotherm equation for a porous solid (equation 6), and the details are given in Appendix 1. Equation (2) used by Nicholson [51] and He and Seaton [52] is different from our equation (7) in that the appropriate weighting factor to calculate the isosteric heat of a porous solid is the change of the density of each

pore with pressure rather than the density of each pore as suggested by them. Their equation is incorrect, because as we have mentioned in our introduction, at high pressures where the small pores are completely filled, the heat released is mainly due to the adsorption in larger pores. Equation (2) indicates a significant contribution from small pores to the heat, which is physically incorrect. On the other hand, our equation shows that at high pressures when small pores are filled, the rate of change of the pore density with respect to pressure in these pores is practically zero and therefore the heat released is purely due to the contributions from larger pores as one would expect physically.

The correct equation for the isosteric heat of a porous solid (as given in equation (7)) involves the derivative of density with respect to pressure. This can be obtained directly from the GCMC simulation, instead of numerically calculating the slope of the isotherm. Starting with the derivative of the ensemble average of the number of particle with respect to (wrt) chemical potential [71] in the Grand Canonical ensemble

$$\frac{\partial\langle N\rangle}{\partial\mu} = \frac{\langle N^2\rangle - \langle N\rangle^2}{kT},$$

we can derive the change of density wrt pressure by applying the chain rule of differentiation

$$\frac{\partial\langle\rho\rangle}{\partial p} = \frac{1}{V}\frac{\langle N^2\rangle - \langle N\rangle^2}{kT}\frac{\partial\mu}{\partial p}.$$

The last factor in the RHS of the above equation can be obtained from the equation of state of the fluid, or it can be obtained from the GCMC simulation of the bulk fluid. In the special case of an ideal gas, the above equation is simplified to:

$$\frac{\partial\langle\rho\rangle}{\partial p} = \frac{\langle N^2\rangle - \langle N\rangle^2}{pV} \tag{8}$$

Thus from the GCMC simulation of adsorption in pores, we can readily compute directly using the above fluctuation formula for the change of density wrt pressure, which then can be used directly in equation (7), without the need to numerically determine the derivative of the isotherm. Figure 1 shows a typical isotherm of argon at 87.3 K in a 8 A slit pore, and the inset shows the derivative of the pore density with respect to pressure. The Henry constant (this slope at zero loading) is about 50 kmol/m^3/Pa is much less than the maximum (which is about 250 kmol/m^3/Pa), and this indicates the importance of fluid–fluid interaction in adsorption. When we obtain the slope of the isotherm in figure 1 by using differential numerical means, the result practically agrees with the slope obtained directly from the MC simulation (equation 8).

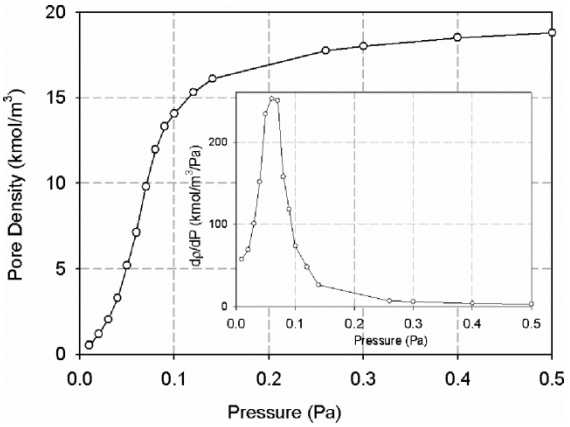

Figure 1. Adsorption isotherm of argon in 8 A slit pore at 87.3 K. The inset shows the slope of isotherm wrt *P*.

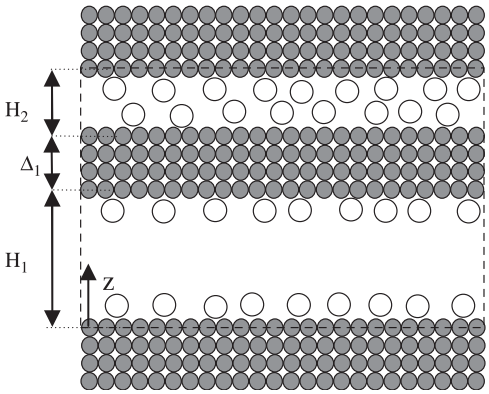

Figure 2. Schematic diagram of the system of two pores of different sizes. The simulation box is bounded by the dashed line.

4.1 Justification of the correct formula with the direct Monte Carlo simulation

To demonstrate the correct formula for the heat of adsorption in a porous solid (equation 7), we carry out the GCMC simulation for a simple system containing two pores stacked together as shown in figure 2. There is no connectivity between these two pores, and this is what equation (7) implies. The pore widths are H_1 and H_2. These two pores are separated by a distance Δ_1, which is chosen to be greater than the cut-off radius so that there is no interaction between the molecules in one pore and those in the other pores to ensure the interdependence of the two pores. In this paper we choose the box length to be ten times the collision diameter and $\Delta_1 = 20$ A. The simulation box, which encompasses both pores, is defined by the dashed line as shown in the figure. The simulation is carried out in a usual manner, with the two basic moves in the creation of configurations. The first move is the displacement of particle and the second move is the insertion/removal step with equal probability between the insertion and removal.

We compute the heat of adsorption for the following sets of pore widths:

Set	H_1 *(A)*	H_2 *(A)*	*Remarks*
1	7	8	The ranges of adsorption are distinct; no phase transition
2	10	12	The ranges of adsorption overlap; phase transition in smaller pore, 10 A
2	8	16	The ranges of adsorption are distinct; phase transition in larger pore, 16 A

The first set is the case where we have no transition pressure in either pore. The second case is the set in which the smaller pore, 10 A, has a transition, while in the last set the transition occurs in larger pore, 16 A.

The isosteric heat released from the adsorption into this set of two pores is obtained from the MC simulation of the two-pore system, and is calculated from equation (1). This heat will be compared with the heat obtained from equation (7), that uses the heats derived from two separate simulations, one which is for the pore H_1 and the other is for pore H_2. The two-pore system of pore H_1 and pore H_2 is denoted hereafter "two-pore (H_1, H_2) system", for example a system of 7 and 8 A pores is "two-pore (7,8) system".

4.1.1 Two-pore (7, 8) system. Figure 3(a) shows the MC isotherm of the two-pore system of 7 and 8 A (half-filled symbols). Since the onset and completion of adsorption in these pores occur over two different ranges of pressure, we see the distinct two stages as reflected by the two peaks in the plot of the slope of isotherm versus pressure (dashed line). The first stage is due to adsorption in 7 A pore while the second is due to the 8 A pore. The solid line in figure 3(a) is the result of equation (6), which uses the individual isotherms of 7 and 8 A pores. The two-stage uptake is also reflected in the isosteric heat of adsorption versus loading as shown in figure 3(b) (half-filled symbols). The first stage in the isosteric heat (due to adsorption in 7 A pore) has a linear increase in the region of loadings less than 10 kmol/m^3, beyond which the isosteric heat decrease which is due to the switch of adsorption to the larger pore (8 A), which has lower solid–fluid energy compared to the smaller pore (7 A). Further increase in loading results in an increase in the heat of adsorption, and this is due to the fluid–fluid interaction in the larger 8 A pore. There is a large fluctuation in the isosteric heat at very high loadings ($>$24 kmol/m^3), and this is due to the difficulty in the insertion of particle into already dense adsorbed phase. Increasing the cycles in the MC run only helps to reduce the fluctuation marginally.

The solid line in figure 3(b) is the calculated results using the correct equation (7) for the isosteric heat, while the dashed line in the same figure is plotted from those using the incorrect equation (2). It is clear that the incorrect equation (2) over-predicts the heat of adsorption in the region where the adsorption in smaller pore (7 A) has been completed. This is so because equation (2) still counts the contribution of this smaller pore in the calculation. On the other hand, our equation (7) correctly captures the behavior of isosteric heat versus loading over the entire course of adsorption.

To show the contribution of individual pores, we show their individual isotherms and the composite isotherm (calculated from equation (6)) in figure 4(a). While the individual heats and combined heats (calculated from equation (7)) are shown in figure 4(b) as a function of pressure. The MC isotherm obtained from the two-pore system (circle symbols) is also shown in the same figure, and it is seen that the agreement between the MC-isotherm of the two-pore system and the calculated isotherm from equation (6) is excellent as one would expect. Now we turn to isosteric heat and this is shown in figure 4(b), where the isosteric heats of individual pores (7 and 8 A) are shown as the dashed line and the dot–dashed line, respectively.

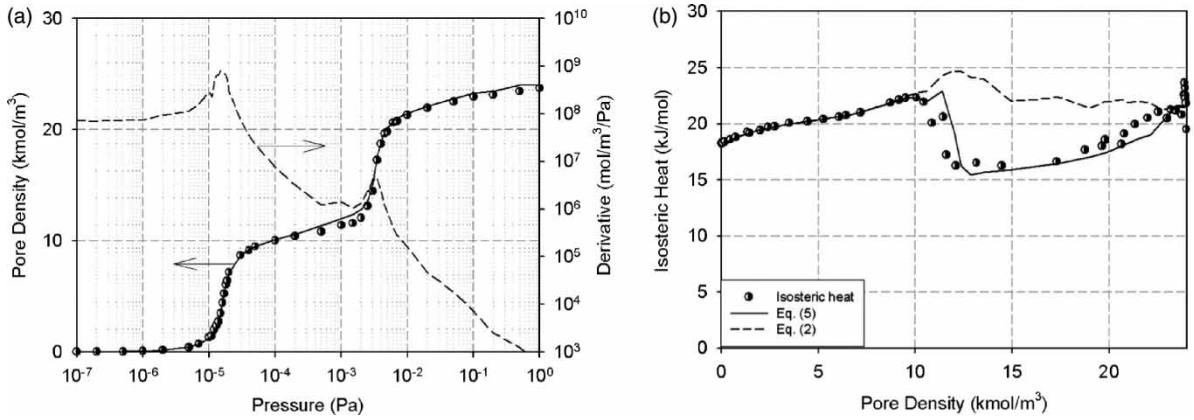

Figure 3. (a) Behavior of adsorption isotherm and isosteric heat in two-pore (7,8) system for adsorption of argon at 77 K (half-filled symbols are from the MC simulation of the two-pore system; the solid line is the calculated result from equation (4), using the individual isotherms of 7 and 8 A pores; the dashed line is the slope of the isotherm of the two-pore system); (b) isosteric heat versus pore density (symbols are from the MC simulation of the two-pore system; the solid line is the calculated result from equation (5); the dashed line is the calculated result from equation (2).

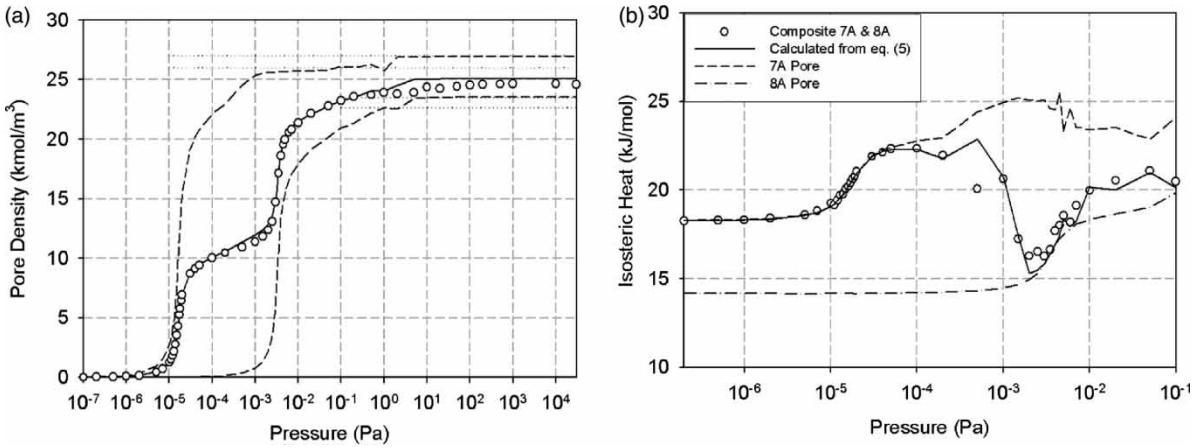

Figure 4. (a) Individual isotherms of 7 and 8 A pores (dashed lines), the composite isotherm of (7, 8 A) pore system (circle symbols), and the isotherm calculated from equation (4) (solid line); (b) isosteric heat of individual 7 A (dashed line) and 8 A pores (dot–dashed line), isosteric heat of composite two-pore system (circle symbols), the isosteric heat calculated from equation (5) (solid line).

The composite isosteric heat, calculated from equation (7), is shown in the same figure as the solid line. The direct simulation results of the two-pore system are presented as circle symbols, and they agree well with the solid line calculated from equation (7), justifying that this equation is the correct equation to compute the composite isosteric heat of a porous solid.

4.1.1.1 Compression of the adsorbed phase

One feature that we note in figure 4(a) is the compression of the individual isotherms, which is clearly identified as the small but sharp jump in the adsorption density after the saturation seems to occur in each pore. The magnitude of this transition is highlighted with two dotted lines as shown in figure 4(a). To show this compression we plot the density distributions at pressures just before and after the compression (figure 5).

For the 8 A pore figure 5(a), and this compression is due to the re-ordering of adsorbed molecules to give better packing in the adsorbed phase. This is reflected in the higher peaks and lower trough in the density versus distance plot. In the case of 7 A pore, where only one layer is possible, the density plots for two values of pressure, one at just before the transition and the other is after, are shown in figure 5(b). Again, the compression is due to the re-ordering of molecule which results in a sharper peak.

4.1.2 Two-pore (10,12) system. Next we show the two-pore system of 10 and 12 A pores. The individual isotherms of 10 and 12 A pores are shown in figure 6, and here we plot the isotherm (top), the slope of the isotherm (middle) and the isosteric heat (bottom) versus pressure. In the case of 10 A pore, two molecular layers are possible, and the sharp transition in this pore is due to the condensation of these two layers. This transition is very sharp in this pore because of the favorable combined solid–fluid and fluid–fluid interactions. The perfect packing in this pore can be seen in the heat contributed by the solid–fluid interaction (solid line in bottom graph

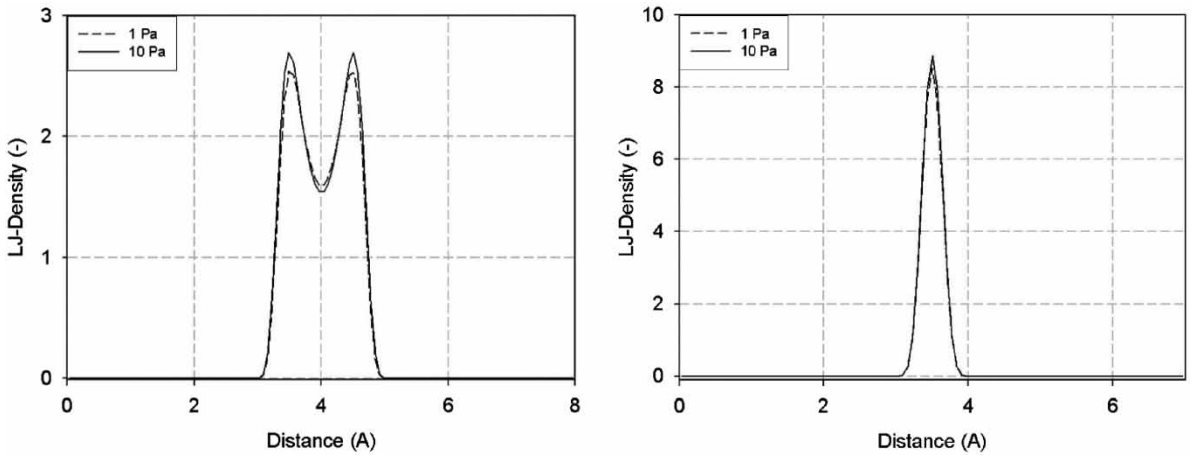

Figure 5. (a) Density plots versus distance at pressures just before and after the transition due to compression for 8 A pore; (b) density plots versus distance at pressures just before and after the transition due to compression for 7 A pore.

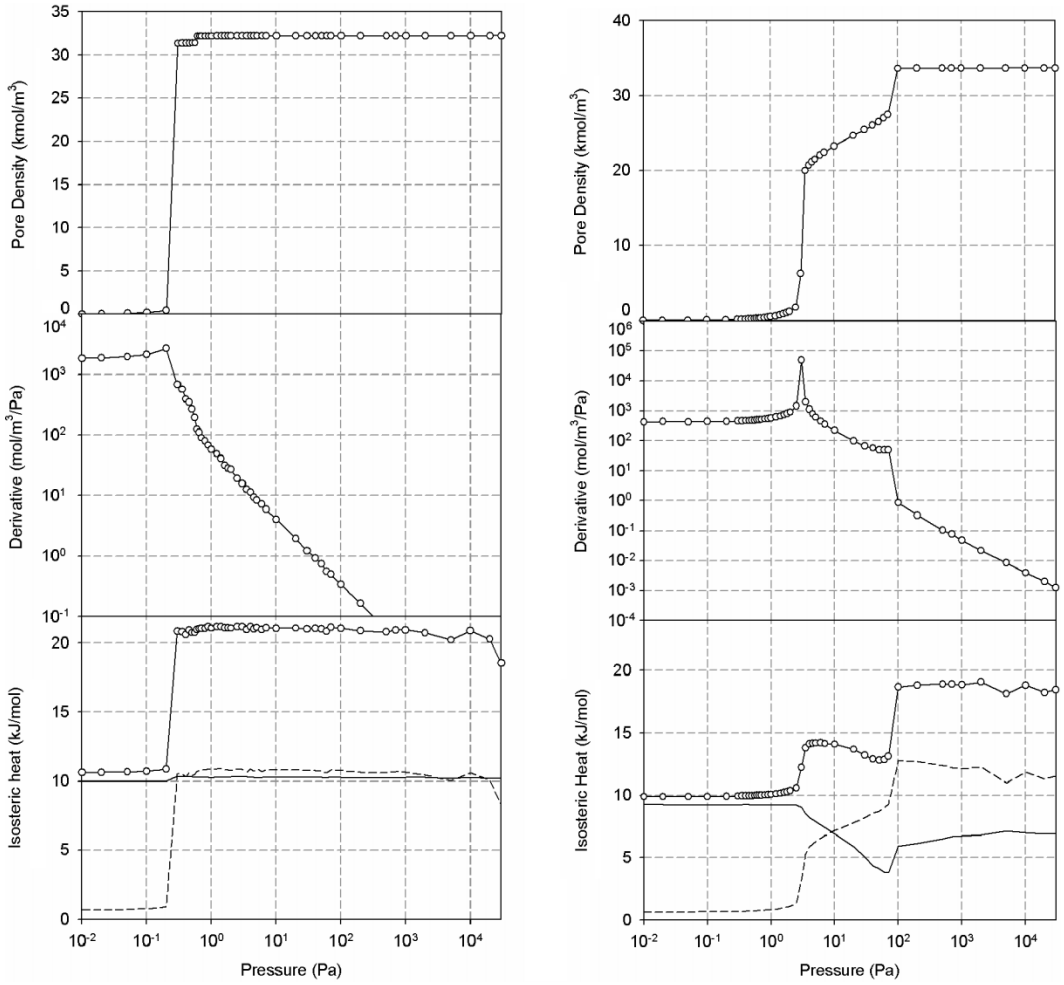

Figure 6. Individual adsorption isotherms of 10 and 12 A pore. The top plot is the isotherm, the middle plot is the slope of the isotherm and the bottom plot is the isosteric heat (the solid line is the contribution from solid–fluid interaction and the dashed line is from the fluid–fluid interaction).

of figure 6(a), which is practically constant, suggesting the adsorbate molecules reside at a constant distance from the solid surface. The sharp increase in the density is also associated with the sharp increase in the heat, which is contributed entirely by the fluid–fluid interaction (dashed line of the bottom graph).

In observing the slope of the isotherm (second graph of figure 6(a)) we see a modest increase before the condensation pressure is reached and this is due to the fluid–fluid interaction. When the condensation is reached there is sharp change in the slope, and then the decrease in the slope very sharp, indicating a plateau in adsorption density has been reached. Further increase in pressure results in a further decrease in the slope and the slope behaves like 1/p (reflected in the slope of minus unity in the log–log plot). This means that as the pressure approaches the vapor pressure the change of the amount with respect to pressure is inversely proportional to $1/p_0$, i.e. the adsorbed phase can still be further compressed at pressures beyond the vapor pressure.

Let us now consider the 12 A pore. The isotherm shows a two-stage uptake—the first stage starts about 3 Pa while the onset of the second stage is about 70 Pa. The first stage is associated with the build-up of the two contact layers close to the surfaces, and the second stage is the complete filling of the pore with the inner core layer (there are three molecular layers that can be packed in this pore). The isosteric heat shows an initial increase, which is due to the fluid–fluid interaction of particles in the two contact layers. It then modestly decreases, and this is due to the onset of adsorption of the inner core (lower solid–fluid interaction; see the solid line of the bottom graph of figure 6(b)). Shortly afterward the heat sharply increases (about 100 Pa), resulting from the complete filling of the inner core.

Now we address the composite isotherm of the two pore (10,12) system, and this isotherm obtained directly from the MC simulation is shown in figure 7 as circle symbols, while the solid line in the same figure is calculated from equation (6) using the individual isotherms of 10 and 12 A pores. There is no surprise that the agreement is excellent. The isosteric heat obtained from the MC simulation of the two-pore (10,12) system is shown in figure 7(b) as the circle symbols, while the calculated isosteric heat from equation (7) (using individual isotherms, their derivatives wrt pressure and heats) are presented as solid line. It is

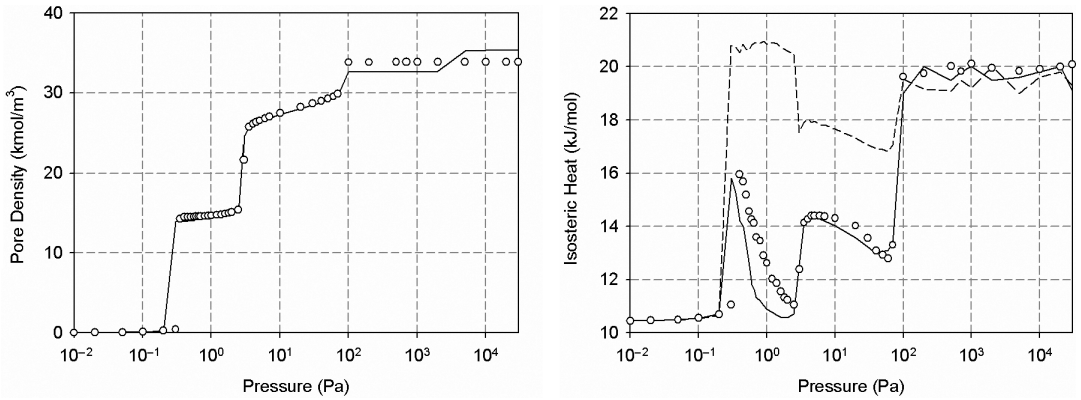

Figure 7. (a) Adsorption isotherm of the two-pore (10, 12) system. The symbols are from the GCMC simulation of the two-pore system, and the solid line is calculated from equation (4) using the individual isotherms of 10 and 12 A pores; (b) isosteric heat of the two-pore (10,12) system. The symbols are from the GCMC simulation of the two-pore system, and the solid line is calculated from equation (5) using the individual isotherms of 10 and 12 A pores while the dashed line is calculated from equation (2).

interesting that the agreement between the two is very good, again confirming the correct formula (equation 7) for the isosteric heat in a porous solid. It is remarkable this equation correctly captures the complex behavior of isosteric heat.

However, if we use the incorrect formula (equation 2) to calculate the isosteric heat, the results are shown in figure 7(b) as the dashed line. It is clear that this result significantly over-predicts the isosteric heat obtained directly from the MC simulation (circle symbols). This significant over-prediction is simply due to the fact that equation (2) still counts the contribution of 10 A pore toward the isosteric heat, despite this pore having been already practically filled. This, yet again proves the incorrectness of equation (2) in the computation of isosteric heat.

4.1.3 Two-pore (8,16) system. We finally consider the system of 8 and 16 A pores. The smaller 8 A pore can pack two overlapped layers in the pore interior (i.e. the pore is too large for one layer and too small for two layers), while the 16 A pore can accommodate four integral layers at saturation. The agreement between the MC heat of the two-pore system (circle symbols) and the calculated results from the correct equation (equation 7) (the solid line) is excellent (figure 8(a)). The failure of the incorrect equation (equation 2) is clearly seen (see the dashed line). It is interesting to observe the complex pattern of the isosteric heat, even for this simple system of two pores. Observing the shape of the isosteric heat of the two-pore system, we identify the seven different regions (labeled as A–G in figure 8b). Let us describe these regions separately.

Region A: Adsorption mainly occurs in 8 A pore. The increase in heat in this region is due to the fluid–fluid interaction (see the dot–dashed line).
Region B: The relative constancy in the heat is due to adsorption in relatively filled 8 A pore.
Region C: The decrease in heat in this region is due to the lesser molecules going into 8 A pore while 16 A starts to uptake molecules.
Region D: Adsorption is increasingly occurred in the two contact layers of 16 A pore and the increase in heat is due to the fluid–fluid interaction in this pore.

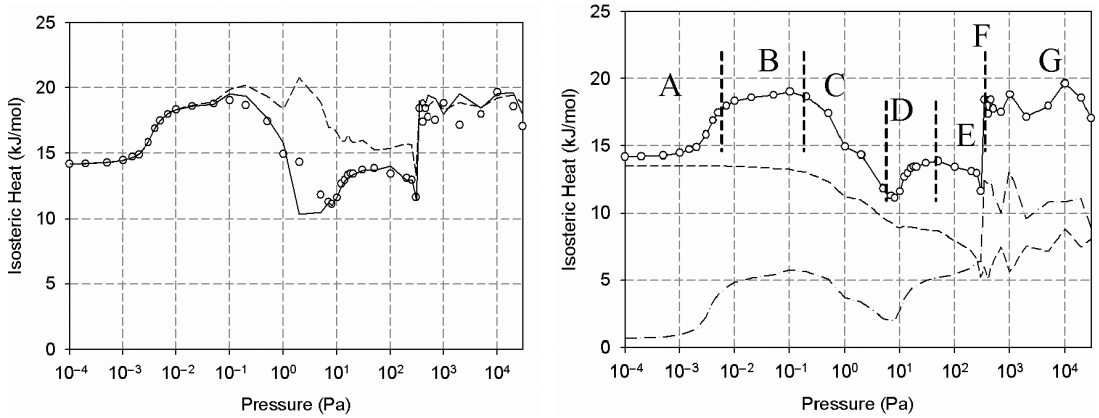

Figure 8. Isosteric heats in the two-pore (8,16) system. The circle symbols are results from the MC simulation of the two-pore system. (a) The solid line is from equation (5) and the dashed line is from equation (2). (b) The dashed line is the contribution from the solid–fluid interaction and the dash-dotted line is from the fluid–fluid interaction.

Region E: The heat has a small decline because adsorption starts to occur in the inner core of the pore where the solid–fluid interaction is lower.
Point F: The sharp jump in the isosteric heat is due to the capillary condensation.
Region G: The relative constancy is due to adsorption in relatively filled 16 A pore.

This complex behavior seen in this simple two-pore system suggests that the pattern of isosteric heat curve for a general porous solid is a complex function of many factors, and as such it is difficult to decompose the heat curve into contributions of various factors affecting adsorption. What this means is that one can not use the isosteric heat curve to derive the PSD as done by He and Seaton [73]. Rather, one should use both the isotherm and heat of adsorption to derive this information. We will show this in the next section with argon and nitrogen adsorption data on S600H and S84 Saran charcoals.

5. Results and discussions

In this section, we apply the correct formula for the heat of adsorption to analyze the experimental results of argon and nitrogen adsorption in activated charcoal. Unfortunately, the data available in the literature on isosteric heat versus loading in porous solids is relatively scarce. The data of Beebe, Millard and Cynarski [5] are available for adsorption of argon and nitrogen at 77 K on Saran charcoal S600H and S84. Their data on the isosteric heat versus loading is very interesting and they exhibit the behavior that is qualitatively observed in the two-pore simulations that were discussed in the last section. The characteristics of Saran charcoal S600H and S84 [86] are given in the following table.

Carbon	*Source*	*Process*	*Physical properies*	*Remark*
S600H	Saran (polyvinyl chloride plastic)	Carbonization (weight loss is 75%) and subsequent hydrogen treatment, both at 600°C.	$V = 0.325$ cc/g $S = 700\,m^2/g$	According to Pierce the pore can only accommodate at most 2 layers
S84	S600 H	Steam activation of S600H at 900 C until a weight loss is 84%	V = 1.1 cc/g $S = 2700\,m^2/g$	From the steam activation the pore volume is increased from 0.325 to 1.1 cc/g

5.1 Local isotherms of argon and nitrogen at 77 K in defective pores

The activated charcoal is expected to contain pores of various sizes and its pore walls are expected to contain defects. This is a more reasonable than the assumption of graphitic walls that is commonly used in the literature. In the absence of any independent information, we will assume that the extent of defect is 30% and the effective defect radius is twice the carbon–carbon bond length (2.84 A). Having defined the pore wall characteristics, we carry out the GCMC simulations for pores of various sizes at 77 K (isotherms as heats versus pressure of these pores are shown in Appendix 2, and then the isotherm and the heat of adsorption of an activated charcoal can be calculated from equations (6) and (7), respectively.

5.2 Comparison with experimental data

The local isotherms obtained in Section 5.1 are used in equations (6) and (7) to obtain the isotherm and heat of adsorption of Saran charcoals. These theoretical isotherm and heat are then used to match against the experimental data to derive the PSD. The experimental data of isotherm and heat for argon are shown in figure 9 as circle symbols, while those for nitrogen are presented in figure 10. The empty symbols are for S84 charcoal and the half-filled symbols are for S600H. For both adsorbates, the isotherm data for S600H at low pressure is not reliable, but its saturation capacity can be used to determine the total pore volume.

While the isotherm data are not sufficiently accurate at low pressures, but the isosteric heat and the isotherm over the region where the data is reliable provide interesting information to test the theoretical model of defective pores. The isosteric heat of S600H is higher than that of S84, indicating that S600H is microporous and the solid–fluid potential in small pores can be twice as high as that in larger pores. Indeed, according to Pierce *et al.* [86], the S600H sample is microporous, while S84 contains larger pores in the micro–mesopore range.

5.2.1 Fitting of the argon data

5.2.1.1 S84. Let us start with the argon adsorption data on S84. The isotherm and heat data are reasonable and they are suitable to be used in the fitting against the GCMC simulation results. Using both the isotherm and heat data of argon adsorption in the fitting, the derived PSD is presented as specific pore volume versus pore width in figure 11(a) (top graph). The fitting is carried out with an optimization routine (*fmincon*) in MatLab. The sum of pore volumes of these pores is $1.1\,cm^3/g$, which is identical to that reported experimentally. Having the pore volume distribution, it is possible to calculate the geometrical surface area and we find a surface area of $1300\,m^2/g$, which is much less than the

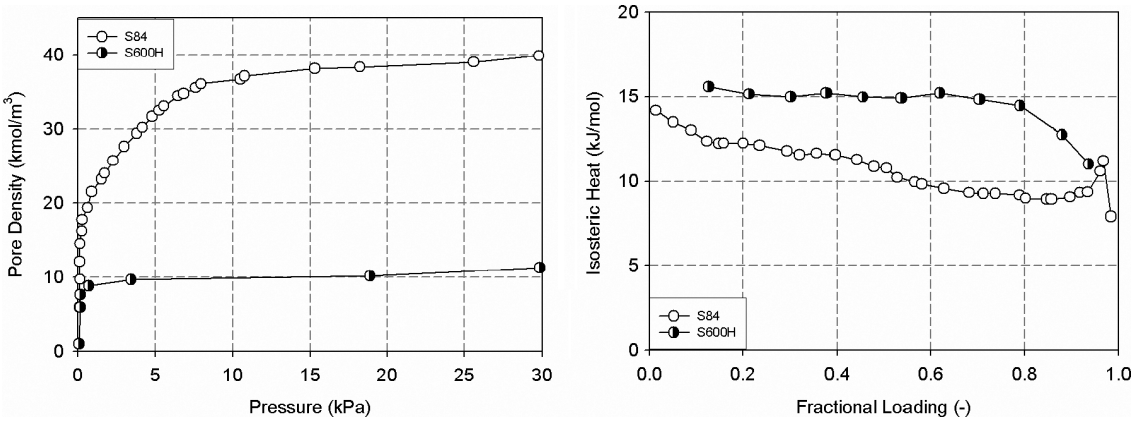

Figure 9. Isotherm and isosteric heat of adsorption of argon in S600H and S84 Saran charcoal at 77 K. The empty circles are for S84 charcoal, and the half-filled symbols are for S600H.

BET surface area of 2700 m^2/g. As is well known in the literature, the BET surface area does not represent the correct surface area because it embeds pore filling in small pores [85].

We see that the pore range of this sample S84 is between 10 and 40 A (with the majority between 10 and 25 A), which is in agreement with the statement made by Pierce that this sample is a micro–mesoporous solid. Pierce *et al.* [87] measured water isotherm and by comparing the onset of water adsorption of this sample against water adsorption on a series of well-defined ACF [87–90], the dominance of pores in the range between 10 and 25 A is indeed confirmed. This is consistent with the preparation of S84, which is the result of activation of S600H with steam, and such an activation process would widen existing micropores and coalescence of these pores.

The isotherm and heat of adsorption are shown in figure 12 with the data shown as solid lines and the GCMC fitted results as half-filled circle symbols. The initial decrease of the isosteric heat is due to the very high surface heterogeneity, which we have seen that the surface heterogeneity can dominate the fluid–fluid interaction (such as 10 A pore and larger pores in figures A2.1 and A2.2). The sharp rise at the end is due to the capillary condensation in larger pores, and a sharp decrease at very high loadings is due to the increased repulsion of particles under dense conditions.

It is important that to reliably derive the PSD we must use as much information as possible, for example using both the isotherm and heat curves, which is exactly what we did here. Since the heat curve carries the information of the temperature dependence of adsorption isotherms, using the fit of theoretical results and isotherms at various temperatures is the same as using the isotherm and heat curve. If we use only either the heat curve or only one isotherm in the derivation of PSD, the result might not be reliable. Let us illustrate this point by considering only the heat curve. The resulted PSD is shown in the middle graph of figure 11 and the fitted results of isotherm and heat are shown as open circle symbols in figure 12. The fit of heat curve is reasonable (expected because we use it in the fitting), while the isotherm is badly described. As seen in figure 11, the PSD for this case is different from that derived earlier (top graph of the same figure) when we used both isotherm and heat curves in the fitting. The same conclusion is obtained if we use only the isotherm in the fitting, from which the derived PSD is shown in figure 11c. We see that the PSDs derived from the fitting against heat only or isotherm only are different from the one derived from the fitting against both isotherm and heat.

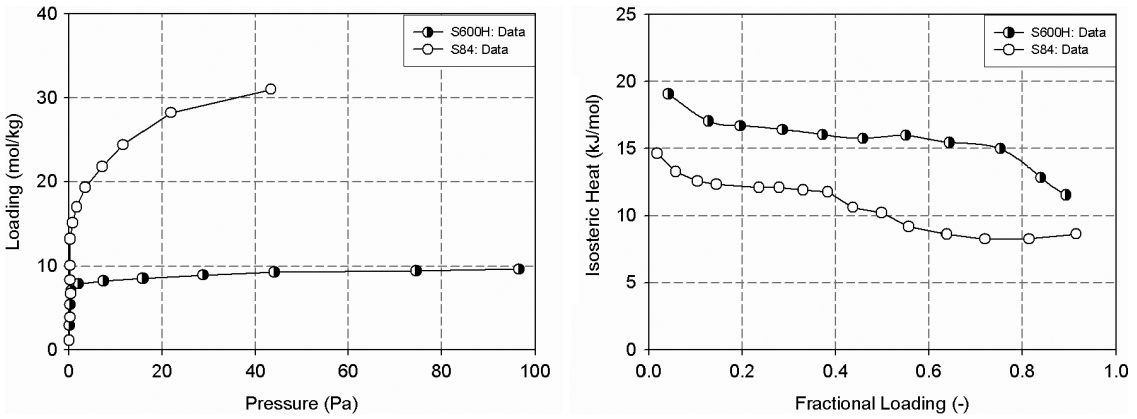

Figure 10. Isotherm and isosteric heat of adsorption of nitrogen in S600H and S84 Saran charcoal at 77 K.

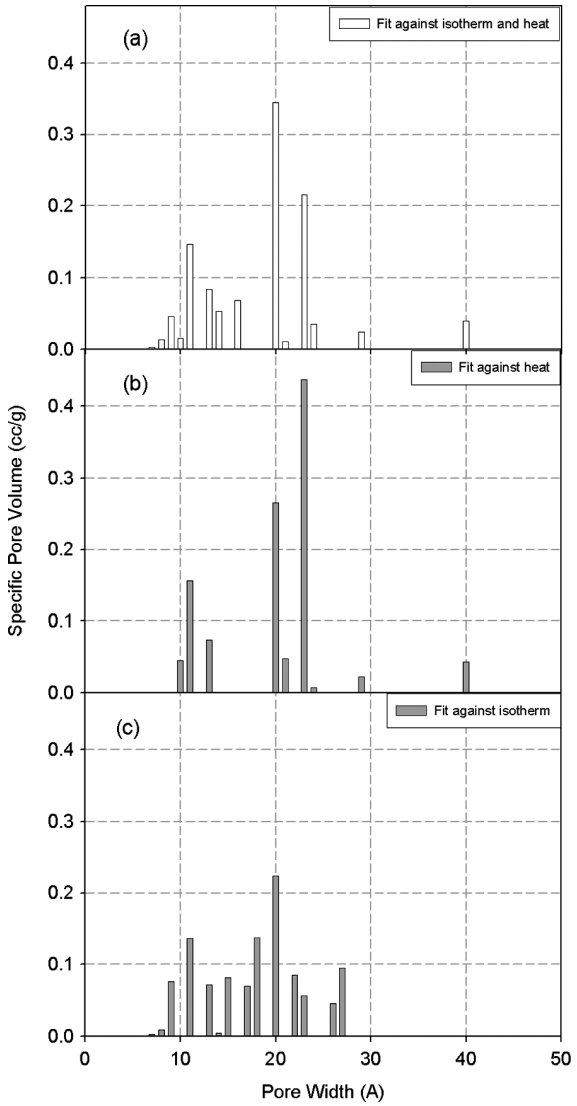

Figure 11. PSD derived from the fitting with (a) isotherm and heat curves, (b) heat curve only and (c) isotherm curve only. The scales of the *y*-axis of these plots are the same to compare the magnitude of the specific volumes.

The GCMC results describe correctly the heat curve. The continual decrease up to 80% of loading is due to the dominance of the surface heterogeneity in all pores, and the sharp rise at about 90% loading is due to the capillary condensation in 20 A pore. The contribution of 20 A pore is shown in figure 12(b) as dashed line with grey symbols. The GCMC results correctly describe this rise, but the extent of this rise is greater than that observed experimentally. It is not possible at this stage to explain this difference as there are many factors that could contribute to this, for example the accuracy of the data, the lack of enough data point, the assumption of the surface defect characteristics. We believe there is a real need for more reliable data before one can have better insight into a given system.

5.2.1.2 S600 H

Let us now turn our attention to the other solid sample, S600H. The isotherm and heat data of argon adsorption on this sample are shown in figure 9 as half-filled symbols. The isotherm is lower than that of S84, but the affinity is greater and so is the heat. This indicates that this sample has lower pore volume and pores are smaller in the sense that the solid–fluid potentials of the two walls overlap, resulting in stronger affinity and higher heat. The heat curve shows an initial decrease for loadings up to about 10%, and this is due to the surface heterogeneity. Between 10% and 70% of loading, the isosteric heat remains practically constant, which is resulted from a balance between the surface heterogeneity and the fluid–fluid interaction, and this is in concert with the results of 7 and 8 A (figures A2.1 and A2.2) pores that we have seen earlier with GCMC simulations. When the loading increases beyond 70% of saturation, we observe a decline in the isosteric heat, which is due to the repulsion among adsorbed particles under dense conditions.

The isotherm of argon in S600H is very sharp at low pressures and the data derived from the graph of the original paper is not very reliable. Therefore the isotherm data can only be used to determine the pore volume. Nevertheless, we proceed formally and from the simultaneous fitting of the isotherm and heat of adsorption

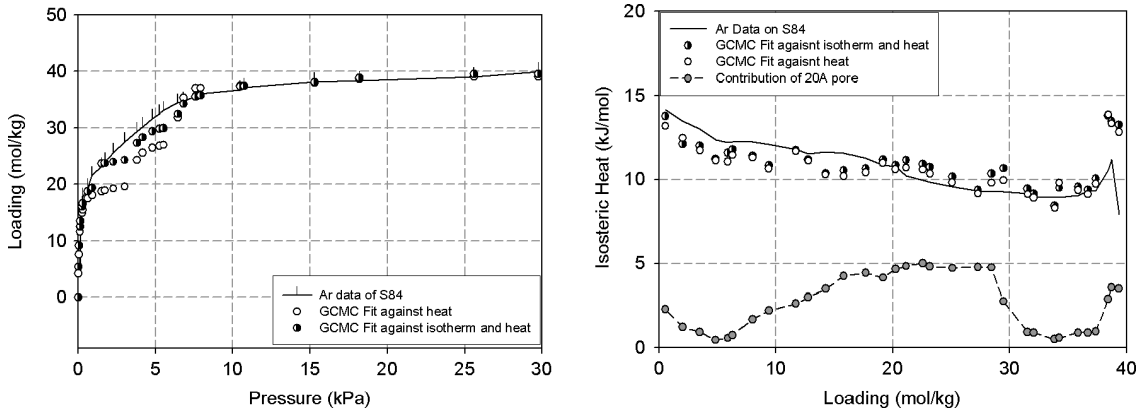

Figure 12. Fit of adsorption and heat between the GCMC results and the experimental data of argon adsorption in S84 at 77 K.

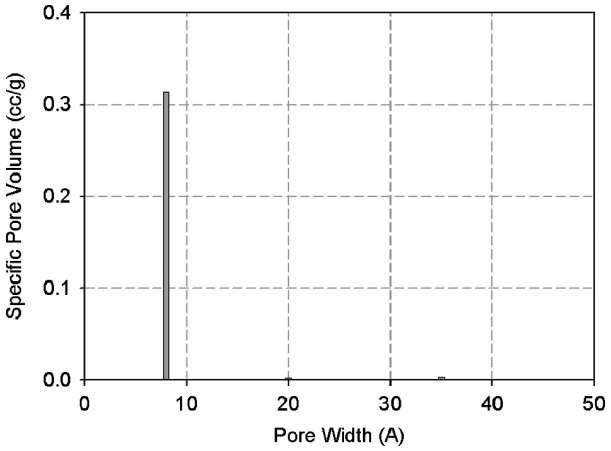

Figure 13. PSD of S600H obtained from the fitting of argon adsorption data.

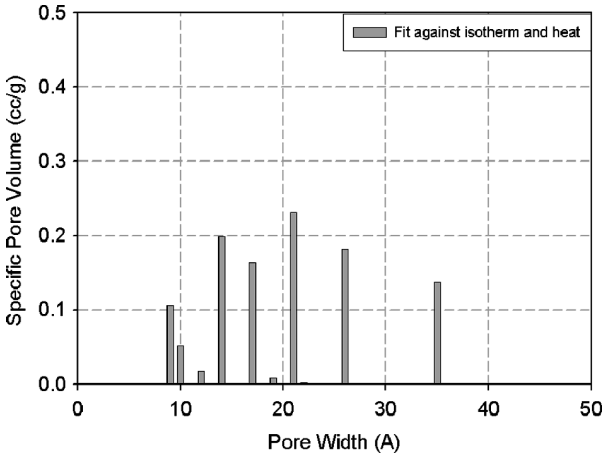

Figure 15. PSD derived from the fitting nitrogen data at 77 K with isotherm and heat curves.

we derive the pore volume distribution (figure 13), from which the pore volume is found to be 0.32 cm^3/g. This is comparable to 0.325 cm^3/g measured experimentally [86]. The pore volume distribution is very narrow with 98% of pores in the neighborhood of 8 A, in which at most two layers that can be packed in this pore. Pierce [86], using the argument of point B in the isotherm being close to the saturation value, concluded that this sample S600H can only accommodate at most two molecular layers. Our analysis indeed justifies his argument.

The fit between the GCMC theoretical results and the experimental data for isosteric heat is shown in figure 14. It is seen that the agreement is very good up to 90% of loading. The drop in the experimental heat at high loadings could be due to the presence of large pores that were not detected from the fitting with the GCMC theoretical results.

5.2.2 Fitting of nitrogen data. We have obtained the PSD of S84 and S600H using argon adsorption data (isotherm and heat). To validate these PSD, we turn to the adsorption data of nitrogen and test whether they are independent of the type of adsorbate used because the PSD should be a function of solid only. By fitting the isotherm and heat data of nitrogen adsorption in S84, we obtain the PSD which is shown in figure 15. Although the PSD from the fitting of nitrogen data is not exactly the same as that (see figure 11) from the argon data (in the light of errors associated with the experimental data as well as the lack of sufficient number of data points for nitrogen), they both share a remarkable similarity in that the majority of pores are in the range of 10–25 A. The PSD derived from nitrogen data has a peak at 35 A while that obtained from argon data does not have such peak, and we attribute this to the lack of nitrogen data for reduced pressures greater than 0.5 while the argon data extends to pressure close to the vapor pressure.

5.2.3 Fitting of argon and nitrogen data. We suggest that for a reliable determination of PSD we must simultaneously use the adsorption data (isotherm and heat) of many adsorbates at different temperatures. This should allow us to determine the defect characteristics of the pore walls. To show this we carry out the fitting of the

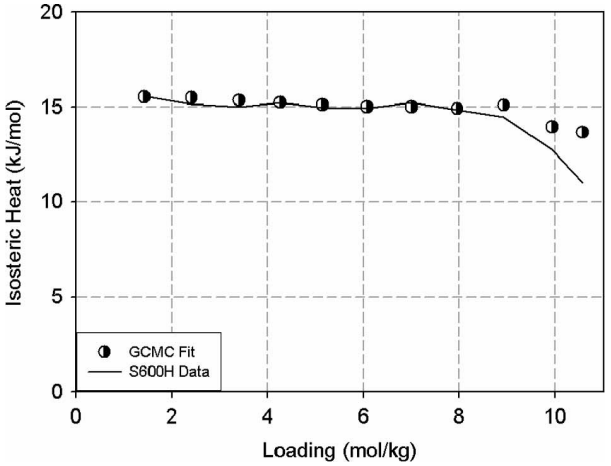

Figure 14. Heat of adsorption of argon in S600H at 77 K (solid line is the experimental data and the open symbols are from GCMC theoretical results).

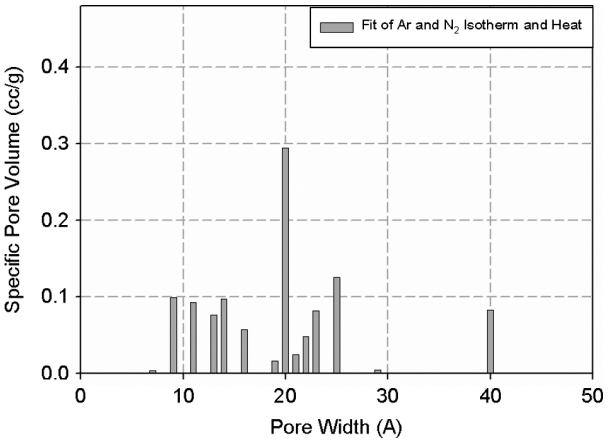

Figure 16. PSD derived from the fitting argon and nitrogen data at 77 K with isotherm and heat curves.

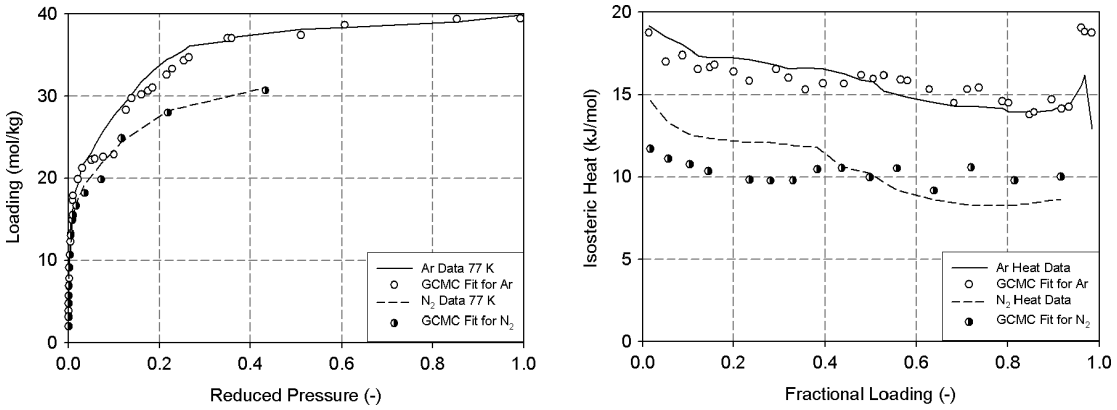

Figure 17. Fit of adsorption and heat between the GCMC results and the experimental data of argon and nitrogen adsorption in S84 at 77 K (the heats of argon are shifted up by 5 kJ for clarity).

isotherm and heat curves of both argon and nitrogen simultaneously, and the results are shown in figure 16 for the pore volume distribution and in figure 17 for the fitted isotherm and isosteric heat. Again we see that the dominance of pores is in the range of 10–25 A, but the distribution is slightly different from those obtained earlier when fitted against either argon or nitrogen data.

5.3 Why defected pore walls are essential?

The analysis carried out so far utilize the local isotherms of pores with defected walls. The question is that why can't we use the conventional model of pores with graphitic wall and avoid the need to use a complex model of defected pore walls? To answer this, we assume the pore walls are graphitic surfaces, and obtain the local isotherms for the pore range as done earlier for defected pores. We take the adsorption of argon in S84 as an illustration. The fit of the GCMC theoretical results and the argon adsorption data (isotherm and heat) results in the PSD shown in figure 18 and the fitted results between the theory and the data are presented in figure 19. The PSD is distinctly different from those (e.g. figure 16) obtained earlier when we used the local isotherms of defected pores. Furthermore the total pore volume for the model of graphitic wall is found to be 0.97 cc/g, which is less than the experimental value of 1.1 cc/g. In contrast, we find that in using the defected pore model, the pore volume is correctly described.

Regarding the fit we see that the isotherm is not described well enough, and neither is the heat curve. In particular we find that the GCMC fit has a greater variation than what we have achieved with defective pore model (compare figure 19(b) with figure 12(b)). This is due to the inherent behavior of heat curve versus loading in perfect pores for which the heat curve increases initially with loading, resulting from the fluid–fluid interaction. While in the case of defective pore model the heat curve decreases initially with loading, resulting from the dominance of surface heterogeneity over fluid–fluid interaction. Typical of heat curves for pores having graphitic walls and those having defected walls are shown in figure 20.

It is concluded that based on the better fit between the data and the defective model we believe that the pore walls of activated carbon are more likely to be defective rather than graphitic. This is in agreement with what has been suggested in the literature [91,92].

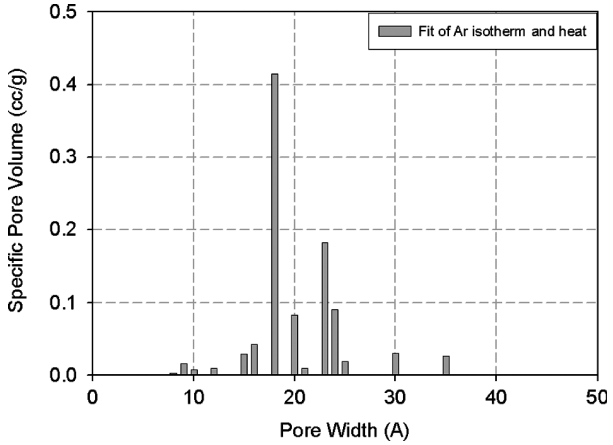

Figure 18. PSD derived from the fitting argon data at 77 K with isotherm and heat curves. Here we use the local isotherms of perfect pores.

5. Conclusions

This paper presents the correct formula for the calculation of the isosteric heat of a porous solid composing of a distribution of independent pores. The formula is justified with the direct MC simulation of a system of two pores. We have tested the formula by fitting the theoretical results against the experimental data of adsorption of argon and nitrogen in Saran charcoal, S84 and S600H. We have found that to derive a more reliable PSD it is recommended that isotherm and heat data of both argon and nitrogen are used simultaneously. We also show that the defected wall model describes the experimental data better than the graphitic wall model, lending support to our

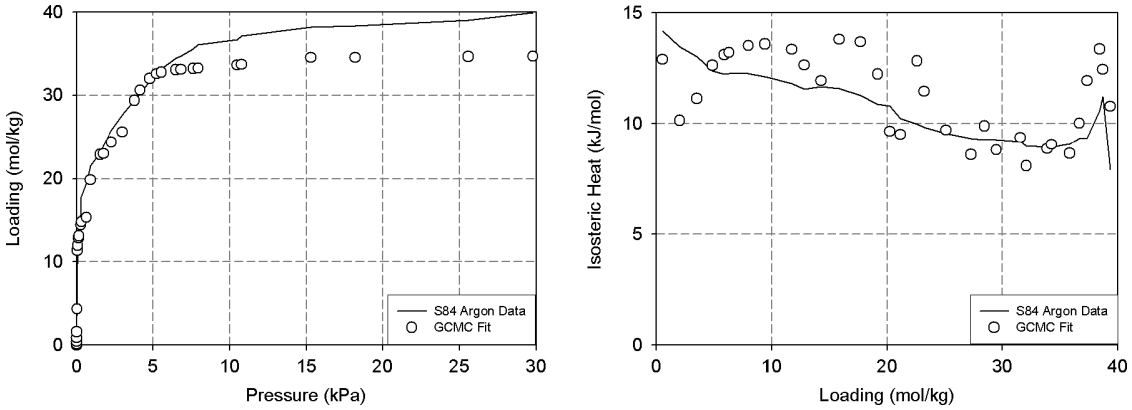

Figure 19. Fit of adsorption and heat between the GCMC results and the experimental data of argon adsorption in S84 at 77 K. Here we use the local isotherms of perfect pores.

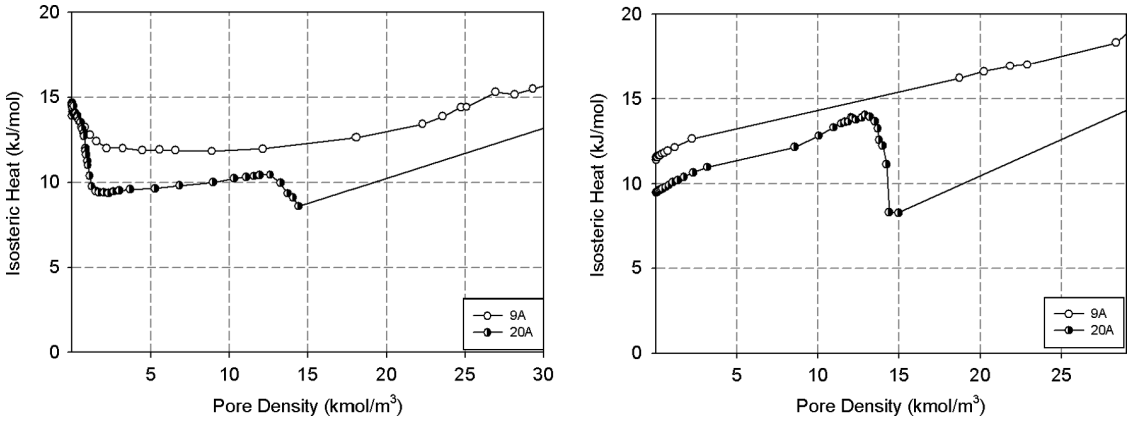

Figure 20. Typical heat of adsorption versus loading for 9 and 20 A pores. (a) Pores with defected walls; (b) pores with graphitic walls.

physical expectation that the pore wall of activated carbon is defected rather than graphitic.

Acknowledgements

This project is supported by the Australian Research Council.

A. Appendix 1

A.1. Derivation of heat equation for a porous solid (equation 7) using the Clapeyron–Clausius equation

Starting with the equation for the amount adsorbed in a porous solid written in terms of local densities in each pore (equation 6; written again here for convenience):

$$\rho(p,T) = \sum_{j=1}^{M} \rho(p,T;H_j)\alpha_j \tag{A1}$$

For a given loading of the porous solid, ρ^*, the pressure and temperature that give this loading are related to each other, according to

$$\rho^* = \sum_{j=1}^{M} \rho(p^*,T^*;H_j)\alpha_j \tag{A2}$$

At a constant loading of the porous solid, we have $\mathrm{d}\rho^* = 0$, and hence the total differentiation of the above equation yields:

$$0 = \mathrm{d}p \sum_{j=1}^{M} \frac{\partial \rho(p^*,T^*;H_j)}{\partial p}\alpha_j + \mathrm{d}T \sum_{j=1}^{M} \frac{\partial \rho(p^*,T^*;H_j)}{\partial T}\alpha_j \tag{A3}$$

Applying the well-established Clapeyron–Clausius equation for the isosteric heat

$$q_{\mathrm{st}}|_{N^*} = q_{\mathrm{st}}(p^*,T^*) = RT^2\left(\frac{\mathrm{d}\ln p}{\mathrm{d}T}\right)_{P^*,T^*}$$

and substituting equation (A3) into the above equation, we get:

$$q_{\mathrm{st}}|_{N^*} = q_{\mathrm{st}}(p^*,T^*) = -\frac{RT^2}{p}\frac{\sum_{j=1}^{M}\alpha_j\left(\frac{\partial \rho_j(p^*,T^*)}{\partial T}\right)}{\sum_{j=1}^{M}\alpha_j\left(\frac{\partial \rho_j(p^*,T^*)}{\partial p}\right)} \tag{A4}$$

Let us take the total differentiation of the local density $\rho_j(p,T)$ and at constant ρ^* the local density is also constant. Therefore

$$\mathrm{d}\rho_j(p^*, T^*) = 0 = \left(\frac{\partial \rho_j(p^*, T^*)}{\partial T}\right)\mathrm{d}T + \left(\frac{\partial \rho_j(p^*, T^*)}{\partial p}\right)\mathrm{d}p \tag{A5}$$

The local isosteric heat at constant ρ_j^* (i.e. at p^* and T^*) is given by the Clapeyron–Clausius equation:

$$q_{\mathrm{st},j}|_{\rho_j^*} = q_{\mathrm{st},j}(p^*, T^*) = RT^2\left(\frac{\mathrm{d}\ln p}{\mathrm{d}T}\right)_{\rho_j^*, P^*, T^*} \tag{A6}$$

Combining equations (A4–6) will give the desired equation (7) in the main text.

B. Appendix 2

Figures A2.1 and A2.2 present the adsorption isotherms and isosteric heat of argon and nitrogen adsorption at 77 K as a function of pressure for pores of different widths, respectively.

With the exception of the smallest pore (7 A) where the heat is fairly constant with loading, all other pores exhibit an initial decline (which is due to the dominance of the surface heterogeneity), followed by the increase (due to the dominance of fluid–fluid interaction including the capillary condensation) and finally a sharp decline at very close to saturation (which is due to the combined decreased in solid–fluid interaction and fluid–fluid interaction).

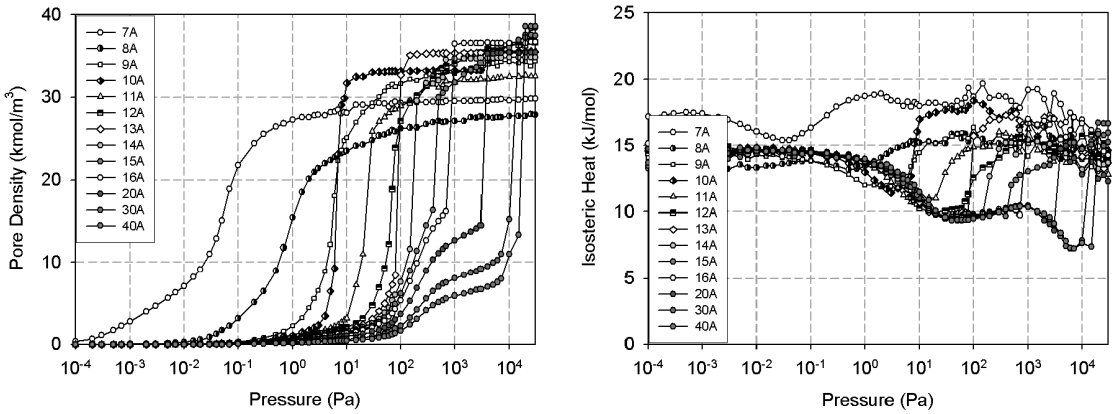

Figure A2.1. Adsorption isotherms of argon at 77 K in defective slit pores of various widths. The extent of defect is 30% and the critical defect radius is 2.84 A.

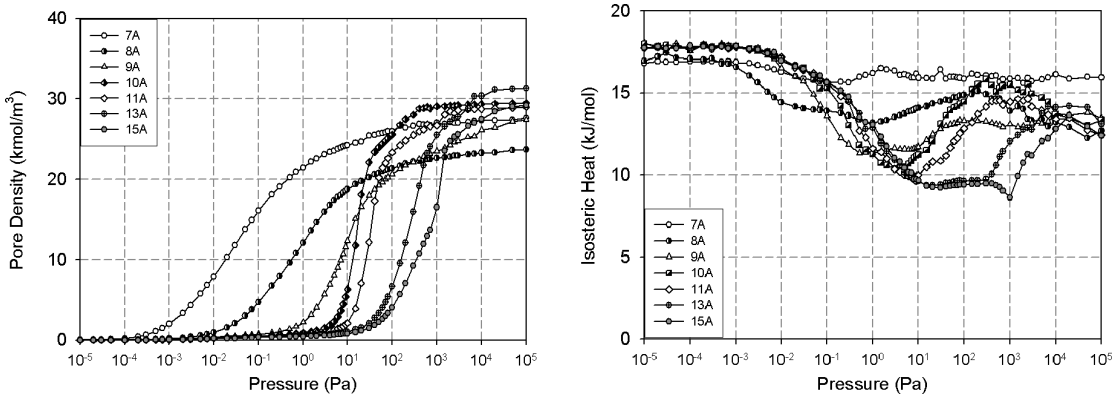

Figure A2.2. Adsorption isotherms of nitrogen at 77 K in defective slit pores of various widths. The extent of defect is 30% and the critical defect radius is 2.84 A.

References

[1] R.A. Beebe, J. Biscoe, W.R. Smith, C.B. Wendell. Heats of adsorption on carbon black. I. *J. Am. Chem. Soc.*, **69**, 95 (1947).

[2] R.A. Beebe, M.H. Polley, W.R. Smith, C.B. Wendell. Heats of adsorption on carbon black. I1. *J. Am. Chem. Soc.*, **69**, 2294 (1947).

[3] W.R. Smith, R.A. Beebe. Heats of adsorption and relative adsorbability of some gaseous hydrocarbons. *Ind. Eng. Chem.*, **41**, 1431 (1949).

[4] R.A. Beebe, G.L. Kington, M.H. Polley, W.R. Smith. Heats of adsorption and molecular configuration. The pentanes on carbon black. *J. Am. Chem. Soc.*, **72**, 40 (1950).

[5] R.A. Beebe, B. Millard, J. Cynarski. Heats of adsorption of nitrogen and argon on porous and on non-porous adsorbents at – 195. *J. Am. Chem. Soc.*, **75**, 839 (1953).

[6] C.H. Amberg, W.B. Spencer, R.A. Beebe. Heats of adsorption of krypton on highly graphitized thermal carbon black. *Can. J. Chem.*, **71**, 305 (1954).

[7] R.A. Beebe, D.M. Young. Heats of adsorption of argon on a series of carbon blacks graphitized at successively higher temperatures. *J. Phys. Chem.*, **58**, 93 (1954).

[8] B. Millard, R.A. Beebe, J. Cynarski. The heat of adsorption of methanol on carbon adsorbents at 0°. *J. Phys. Chem.*, **58**, 468 (1954).

[9] R.A. Beebe, R.M. Dell. Heats of adsorption of polar molecules on carbon surfaces. I. Sulfur dioxide. *J. Phys. Chem.*, **59**, 746 (1955).

[10] R.M. Dell, R.A. Beebe. Heats of adsorption of polar molecules on carbon surfaces. II. Ammonia and methylamine. *J. Phys. Chem.*, **59**, 754 (1955).

[11] W.B. Spencer, C.H. Amberg, R.A. Beebe. A further studies of adsorption on graphitized carbon black. *J. Phys. Chem.*, **62**, 719 (1958).

[12] R.A. Beebe, R.L. Gale, T.C. Kleinsteuber. Calorimetric heats of adsorption of nitrogen, carbon monoxide, and argon on graphon at − 70. *J. Phys. Chem.*, **70**, 4010 (1966).

[13] N.N. Avgul, G.I. Berezin, A.V. Kiselev, A. Korolev. The effect of the porosity of graphite adsorbents on the adsorption and heat of adsorption of hexane vapors. *Coll. J.*, **20**, 283 (1958).

[14] A.G. Bezus, V.P. Dreving, A.V. Kiselev. Isotherms and heats of adsorption of propane and propylene on graphitized carbon black. The energy of the adsorption process. *Coll. J.*, **23**, 389 (1961).

[15] A. Isirikyan, A.V. Kiselev. The absolute adsorption isotherms of vapors of nitrogen, benzene and n-hexane and the heats of adsorption of benzene and n-hexane on graphitized carbon blacks. I. Graphitized thermal blacks. *J. Phys. Chem.*, **65**, 601 (1961); **66** 205 (1962).

[16] N.N. Avgul, A.V. Kiselev, I. Lygina. Isotherms and heats of adsorption of sphere-like molecules on graphitized carbon black. Potential energies and chances in thermodynamic functions upon adsorption on graphite. *Trans. Trans. Farad. Soc.*, **59**, 2113 (1963).

[17] A.V. Kiselev, M.V. Serdobov. Some characteristic correlations between the differential heats of adsorption of benzene, carbon tetrachloride, methyl cyclohexane and perfluoromethylcyclohexane and the coverage of a graphitized carbon black surface. *Russ. J. Phys. Chem.*, **37**, 1402 (1963).

[18] A.G. Bezus, V.P. Dreving, A.V. Kiselev. Energy of adsorption of ethane and ethylene on surfaces of varying nature – Isotherms and heat of adsorption of ethane on graphitized carbon black. *Russ. J. Phys. Chem.*, **38**, 30 (1964).

[19] R.A. Beebe, A.V. Kiselev, N. Kovaleva, R. Tyson, J. Holmes. Adsorption and satte of CO2, SF6 and NH3 on a graphitized carbon surface. I. Adsorption isotherms. *Russ. J. Phys. Chem.*, **38**, 372 (1964).

[20] A. Bezus, V. Dreving, A.V. Kiselev. Adsorption energy of ethane and ethylene on surfaces of varying nature. *Russ. J. Phys. Chem.*, **38**, 511 (1964).

[21] A.V. Kiselev. Short range molecular interaction. *Russ. J. Phys. Chem.*, **38**, 1501 (1964).

[22] A.G. Bezus, V. Dreving, A.V. Kiselev. The isotherms and heats of adsorption of methane on graphitized carbon black. *Russ. J. Chem. Eng.*, **38**, 1589 (1964).

[23] A.G. Bezus, V. Dreving, A.V. Kiselev. Variation with pressure and temperature of adsorption of methane and ethylene on graphitized carbon black. *Russ. J. Phys. Chem.*, **41**, 1568 (1967).

[24] L. Beljakova, A.V. Kiselev, N. Kovaleva. Determination by gas chromatography of adsorption isotherms and heats of adsorption for steam and benzene on graphitized carbon black. *Bull. Soc. Chim. Fr.*, **1**, 285 (1967).

[25] G. Berezin, A.V. Kiselev, R. Sagatelyan, M. Serdobov. Two calorimeter system for measuring adsorption and heat of adsorption. *Russ. J. Phys. Chem.*, **43**, 118a (1969).

[26] G. Berezin, A.V. Kiselev, R. Sagatelyan, M. Serdobov. Heat of adsorption of carbon tetrachloride on a graphitized carbon black above and below 2-dimensional critical temperature. *Russ. J. Phys. Chem.*, **43**, 118b (1969).

[27] G. Berezin, A.V. Kiselev, I. Kleshnina, V. Sinitsyn. Heat capacities of ethyl and tertiary butyl alcohols in adsorption layers on graphitized carbon black. *Russ. J. Phys. Chem.*, **43**, 894 (1969).

[28] G.I. Berezin, A.V. Kiselev, V. Sinitsyn. Adsorption of benzene and normal-hexane on graphitized carbon black. *Russ. J. Phys. Chem.*, **44**, 408 (1970).

[29] N. Avgul, A.V. Kiselev. Physical adsorption of gases and vapors on graphitized carbon blacks. *Chem. Phys. Carbon*, **6**, 1 (1970).

[30] G. Berezin, A.V. Kiselev, R. Sagatelyan, O. Chistozvonova. Adsorption of ethyl-alcohol on surface of graphitized carbon black at various temperatures. *Russ. J. Phys. Chem.*, **46**, 432 (1972).

[31] N. Avgul, A. Bezus, E. Dobrova, A.V. Kiselev. The similarity of gas adsorption by nonporous and microporous crystalline adsorbents. *J. Coll. Int. Sci.*, **42**, 486 (1973).

[32] R. Bekkerova, G. Berezin, A.V. Kiselev. Phase transitions of adsorbed hexane. *Russ. J. Phys. Chem.*, **52**, 141 (1978).

[33] A. Derkaui, A.V. Kiselev, B. Kuznetsov. Calorimetric measurement of heats of vapour adsorption on graphitized thermal carbon black. *J. Chem. Soc. Farad. Trans. I.*, **81**, 1685 (1985).

[34] J. Regnier, J. Rouquerol, A. Thomy. Calorimetric measurements of heat of adsorption of krypton and xenon on graphite at 77 and 87.5 K by means of a continuous introduction of adsorbate. *J. Chim. Phys.*, **72**, 327 (1975).

[35] Y. Grillet, F. Rouquerol, J. Rouquerol. Study of physical adsorption of gases by a continuous procedure. 2. Experimental evidence of phase change of nitrogen adsorbed at 77 K on differently graphitized carbons. *J. Chim. Phys.*, **74**, 778 (1977).

[36] J. Rouquerol, S. Partyka, F. Rouquerol. Calorimetric evidence for a Bi-dimensional phase change in the monolayer of nitrogen or argon adsorbed on graphite at 77 K. *J. Chem. Soc. Farad. Trans. I.*, **73**, 306 (1977).

[37] Y. Grillet, F. Rouquerol, J. Rouquerol. Two-Dimensional freezing of nitrogen or argon on differently graphitized carbons. *J. Coll. Int. Sci.*, **70**, 239 (1979).

[38] J. Rouquerol, F. Rouquerol, Y. Grillet. Energetical aspects of N2 and Ar adsorption: Specific adsorption, two-dimensional phase changes and adsorption in micropores. *Pure Appl. Chem.*, **61**, 1933 (1989).

[39] J. Pikunic, P. Llewellyn, R. Pellenq, K. Gubbins. Argon and nitrogen adsorption in disordered nanoporous carbons: Simulation and experiment. *Langmuir*, **21**, 4431 (2005).

[40] G. Kington, J. Aston. The heat of adsorption of nitrogen on titanium dioxide (Rutile) at 77.3. *J. Am. Chem. Soc.*, **73**, 1929 (1951).

[41] J. Greyson, J. Aston. The heats of adsorption of helium and neon on graphitized carbon black. *J. Phys. Chem.*, **61**, 610 (1957).

[42] J. Aston, J. Wood, T. Zolki. The thermodynamic properties and configuration of unsymmetrical dimethylhydrazine. *J. Am. Chem. Soc.*, **75**, 6202 (1953).

[43] J. Aston, G. Szaz. The Thermodynamics of Butadiene-1,2 from calorimetric and spectroscopic data. *J. Am. Chem. Soc.*, **69**, 3108 (1947).

[44] J. Aston, J. Greyson. Theory of heats of adsorption on a uniform surface. Effect of lateral interaction and grain boundaries. *J. Phys. Chem.*, **61**, 613 (1957).

[45] J. Aston, J. Eidinoff. The low temperature precision adiabatic calorimeter adapted to condensed gases from 10'K. to room temperature. *J. Am. Chem. Soc.*, **61**, 1533 (1939).

[46] J.A. Morrison, J. Szaz. The heat capacity of nitrogen adsorbed on titanium dioxide between 20K and 80K. *J. Chem. Phys.*, **16**, 280 (1948).

[47] J.A. Morrison, J. Los, L. Drain. The heat capacity, integral heat of adsorption and entropy of argon adsorbed on titanium dioxide. *Trans. Farad. Soc.*, **47**, 1023 (1951).

[48] J. Piper, J.A. Morrison, C. Peters, Y. Ozaki. Heats and entropies of adsorption of nitrogen on grafoil at 79.3K. *J. Chem. Soc. Farad. Trans. I.*, **79**, 2863 (1983).

[49] J. Morrison. Calorimetry in the study of physical adsorption. *Pure Appl. Chem.*, **59**, 7 (1987).
[50] C. Peters, J. Morrison, M. Klein. The adsorption of acetylene on a graphite surface:, *Surf. Sci.*, **165**, 355 (1986).
[51] A. Inaba, J. Morrison. Ethylene on graphite: Heats of adsorption and phase diagram. *Phys. Rev. B*, **34**, 3238 (1986).
[52] J. Piper, J. Morrison. Heats of adsorption and vibrational frequencies for xenon adsorbed on graphite. *Chem. Phys. Lett.*, **103**, 323 (1984).
[53] J. Piper, J. Morrison, C. Peters. The adsorption of carbon monoxide on graphite. *Mol. Phys.*, **53**, 1463 (1984).
[54] J. Piper, J. Morrison. Heats of adsorption of methane multilayers on graphite. *Phys. Rev. B*, **30**, 3480 (1984).
[55] L. Drain, J. Morrison. Thermodynamic properties of nitrogen and oxygen adsorbed on rutile. *Trans. Farad. Soc.*, **49**, 654 (1953).
[56] J. Morrison, L. Drain, J. Dugdale. Phase transitions in multi-molecular layers of adsorbed nitrogen. *Can. J. Chem.*, **30**, 890 (1952).
[57] L. Drain, J. Morrison. Interpretation of the thermodynamic properties of adsorbed argon at low surface coverages. *Trans. Farad. Soc.*, **48**, 316 (1952).
[58] L. Drain, J. Morrison. Thermodynamic properties of argon adsorbed on rutile. *Trans. Farad. Soc.*, **48**, 840 (1952).
[59] J. Morrison, L. Drain. The heat capacity of multimolecular layers of adsorbed argon. *J. Chem. Phys.*, **19**, 1063 (1951).
[60] J. Morrison, J. Los. The measurement of the thermal properties of gases and vapours adsorbed on solid surfaces. *Dis. Farad. Soc.*, **8**, 321 (1950).
[61] E. Pace, A. Siebert. Heats of adsorption and adsorption isotherms for low boiling gases adsorbed on graphon. *J. Phys. Chem.*, **64**, 961 (1960).
[62] E. Pace, I. Pierce, K. Dennis. Adiabatic calorimeter for use with condensable gases and gas-solid systems between 10 and 150K. *Rev. Sci. Instr.*, **26**, 20 (1955).
[63] E. Pace, E. Heric, K. Dennis. Some thermodynamic properties of methane adsorbed on rutile between 80 and 140K. *J. Chem. Phys.*, **21**, 1225 (1953).
[64] E. Pace, A. Siebert. Heat of adsorption of parahydrogen and orthodeuterium on graphon. *J. Phys. Chem.*, **63**, 1398 (1959).
[65] R. Bobka, R. Dininny, A. Siebert, E. Pace. Heat capacity and heat of adsorption of argon adsorbed on graphon. *J. Phys. Chem.*, **61**, 1646 (1957).
[66] E. Pace. Argon adsorbed on a graphitic surface. The heat of adsorption from lattice liquid theory. *J. Chem. Phys.*, **27**, 1341 (1957).
[67] E. Pace, W. Berg, A. Siebert. Entropy of krypton adsorbed on titanium dioxide (Anatase). *J. Am. Chem. Soc.*, **78**, 1531 (1956).
[68] E. Pace, K. Dennis, W. Berg. Thermodynamic properties of krypton adsorbed on titanium dioxide (anatase). *J. Chem. Phys.*, **23**, 2166 (1955).
[69] E. Pace, S. Greene. Heat of adsorption of argon adsorbed on titanium dioxide between 60 and 90°K. *J. Am. Chem. Soc.*, **76**, 3286 (1954).
[70] E. Pace, D. Sasmor, E. Heric. Heat capacity of methane adsorbed on titanium dioxide between 55 and 90°K. *J. Am. Chem. Soc.*, **74**, 4413 (1952).
[71] D. Nicholson, N. Parsonage. *Computer simulation and the statistical mechanics of adsorption*, Academic Press, London (1982).
[72] D. Nicholson. A simulation study of energetic and structural heterogeneity in slit-shaped pores. *Langmuir*, **15**, 2508 (1999).
[73] Y. He, N. Seaton. Monte Carlo simulation and pore-size distribution analysis of the Isosteric heat of adsorption of methane in activated carbon. *Langmuir*, **21**, 8297 (2005).
[74] G. Birkett, D.D. Do. Correct procedures for the calculation of heats of adsorption for heterogeneous adsorbents from molecular simulation. *Langmuir*, **22** (2006) In press.
[75] D.D. Do, H.D. Do. Effects of potential models in the vapor-liquid equilibria and adsorption of simple gases on graphitized thermal carbon black. *Fluid Phase Equil.*, **236**, 169 (2005).
[76] D.D. Do, H.D. Do, K. Kaneko. Effect of surface-perturbed intermolecular interaction on adsorption of simple gases on a graphitized carbon surface. *Langmuir*, **20**, 7623 (2004).
[77] D.D. Do, H.D. Do. Adsorption of ethylene on graphitized thermal carbon black and in slit pores: A computer simulation study. *Langmuir*, **20**, 7103 (2004).
[78] L. Gardner, M. Kruk, M. Jaroniec. Reference data for argon adsorption on graphitized and nongraphitized carbon blacks. *J. Phys. Chem. B*, **105**, 12516 (2001); M. Kruk, Z. Li, M. Jaroniec, Nitrogen adsorption study of surface properties of graphitized carbon blacks. *Langmuir*, **15** (1999) 1435.
[79] A. Michels, H. Wijker, H. Wijker. Isotherms of argon between 0 degrees and 150 degrees C and pressure up to 2900 atmospheres. *Physica (The Hague)*, **15**, 627 (1949).
[80] P. Ravikovitch, A. Vishnyakov, A. Neimark. Density functional theories and molecular simulations of adsorption and phase transitions in nanopores. *Phys. Rev. E*, **64**, 011602 (2001).
[81] W.A. Steele. The physical interaction of gases with crystalline solids. I. Gas-solid energies and properties of isolated adsorbed atoms. *Surf. Sci.*, **36**, 317 (1973).
[82] M.P. Allen, D.J. Tildesley. *Computer Simulation of Liquids*, Clarendon Press, Oxford (1987).
[83] D. Frenkel, B. Smit. *Understanding Molecular Simulations*, Academic Press, New York (2002).
[84] D.D. Do, H.D. Do. Modeling of adsorption on nongraphitized carbon surface: GCMC simulation studies and comparison with experimental data. *J. Phys. Chem. B*, **110**, 17531 (2006).
[85] S.J. Gregg, K.S.W. Sing. *Adsorption, Surface Area and Porosity*, Academic Press, New York (1982).
[86] C. Pierce, J. Wiley, R. Smith. Capillarity and surface area of charcoal. *J. Phys. Coll. Chem.*, **53**, 669 (1949).
[87] K. Kaneko, Y. Hanzawa, T. Iiyama, T. Kanda, T. Suzuki. Cluster-Mediated water adsorption on carbon nanopores. *Adsorption*, **5**, 7 (1999).
[88] Y. Hanzawa, K. Kaneko. Lack of a predominant adsorption of water vapor on carbon mesopores. *Langmuir*, **13**, 5802 (1997).
[89] T. Kimura, H. Kanoh, T. Kanda, T. Ohkubo, Y. Hattori, Y. Higaonna, R. Denoyel, K. Kaneko. Cluster-Associated filling of water in hydrophobic carbon micropores. *J. Phys. Chem. B.*, **108**, 14043 (2004).
[90] T. Ohba, H. Kanoh, K. Kaneko. Cluster-Growth-Induced Water adsorption in hydrophobic carbon nanopores. *J. Phys. Chem. B.*, **108**, 14969 (2004).
[91] M. Kruk, M. Jaroniec, J. Choma. Comparative analysis of simple and advanced sorption methods for assessment of microporosity in activated carbon. *Carbon*, **36**, 1447 (1998).
[92] E. Ustinov, D.D. Do, V.B. Fenelonov. Pore size distribution analysis of activated carbons: Application of density functional theory using nongraphitized carbon black as a reference system. *Carbon*, **44**, 653 (2006).